Electron temperature and density profile evolution during the ELM cycle in ohmic and EC-heated H-mode plasmas in TCV

A. Pitzschke,[1, a)] R. Behn,[1, b)] O. Sauter,[1] S. Yu. Medvedev,[2] B. P. Duval,[1] J. Marki,[1] L. Porte,[1] L. Villard,[1] and the TCV team[1]

[1)] *Ecole Polytechnique Fédérale de Lausanne (EPFL), Centre de Recherches en Physique des Plasmas (CRPP), Association Euratom-Confédération Suisse, Station 13, CH-1015 Lausanne, Switzerland*

[2)] *Keldysh Institute of Applied Mathematics, Russian Academy of Sciences, Miusskaya 4, 125047 Moscow, Russia*

(Dated: December 9, 2011)

The dynamics of electron temperature and density profiles during quasi-stationary H-mode phases in the TCV tokamak has been investigated for type III and type I ELMs using electron cyclotron heating (ECH) to vary the collisionality. At heating power levels close to the threshold for the L-H transition, ELMs of type III were observed, with an energy loss per ELM below 10% of the total plasma energy. Electron temperature and pressure showed no significant increase during the phase before the ELM crash. ELMs of type I were characterized by a lower repetition rate, but caused fractional energy losses reaching 20%. For this ELM type, a clear increase in pedestal pressure and pressure gradient was observed before the collapse associated with the ELM event. The rapid drop in electron temperature also affected the plasma core explaining the rather large energy losses per ELM. Ideal MHD stability calculations of the edge pedestal with the KINX code showed that high-n ballooning modes restricted the achievable pressure gradient at high collisionality and ELMs of type III. With additional heating and type I ELMs, stability limits were set by medium-n kink-ballooning modes. Comparing the values of the pressure gradients and current densities obtained from experimental data with those of ideal MHD stability calculations showed good agreement. The model, however, needs to account for the radial displacement of the location of maximum pressure gradient during the ELM cycle.
(Some figures in this article are in color only in the electronic version)

PACS numbers: 28.52-s, 52.55-s, 52.55.Fa, 52.25.Fi, 52.50.Sw, 52.55.Tn, 52.70.Kz

I. INTRODUCTION

Experimental studies and theoretical modeling, aimed at a better understanding of the plasma behaviour near the edge in H-mode scenarios, are of continuing interest. Pilot experiments in thermo-nuclear fusion research, such as ITER, will rely on operation in H-mode providing further motivation. Although a subject of investigation over many years, and on many machines - tokamaks and stellerators - many open questions remain[1–5]. In particular, the dynamic behaviour of the profiles of plasma density and temperature in the edge region, influenced by edge-localized modes (ELMs), deserves further attention. With improved diagnostic capabilities, some of these subjects may now be addressed[6–12] and the experimental results can be compared with the predictions of theoretical models[13–17].

For this study, profiles of electron density and temperature were measured using Thomson scattering with high spatial resolution near the plasma edge[12]. Using repetitively pulsed lasers, the time evolution of the profiles across the ELM cycle has been recorded. Since the inherent repetition rate of the laser is of the same order as the ELM frequency, random sampling and coherent averaging were applied to a number of discharges to reconstruct the time history of a "typical" ELM cycle. For this, a series of reproducible shots with extended quasi-stationary phases and regular ELMs was required. The measured profiles were fitted by an analytical function, following an established procedure[18], to obtain parameters that characterize the pedestal and describe the time evolution.

The electron-cyclotron heating system (ECH) installed on the TCV tokamak[19], was used to perform experiments at different levels of additional heating power. This permitted the comparison of cases at different collisionalities and in consequence different types of ELMs. As usual, the classification of the ELM type is based on the variation of the ELM frequency with input power. The cases with higher collisionalites ($\nu^*_{e,ped} = 0.75$) refer to heating powers close to the threshold for the L-H transition[20], which on TCV may be reached already by ohmic heating. Under these conditions, ELMs of type III are observed. Lower collisionalities ($\nu^*_{e,ped} = 0.4$), and type I ELMs were obtained by additional heating using ECH at the 3rd harmonic. With ECH, heating power is deposited in the plasma center and is coupled to the electrons. It is worth noting that, with ECH as heating method, there is no particle fueling nor direct momentum injection in contrast to plasma heating using neutral beam injection (NBI).

The experimental results are compared with ideal MHD stability calculations (KINX code[21]) using the

[a)] E-mail author: andreas.pitzschke@kkl.ch
[b)] E-mail co-author: roland.behn@epfl.ch

measured pressure profiles as input. In the stability diagram, presented in the parameter space of normalized edge current density versus normalized pressure gradient, points referring to particular experimental conditions can be compared with the predicted stability limits. In both cases considered here, the pedestal resistivity is sufficiently low to justify the analysis based on ideal MHD. During earlier experiments[22] dedicated to the study of small type III ELMs of higher frequency, resistive effects could not be neglected and the stability limits obtained from ideal MHD could not explain the observed ELM behaviour.

This paper is structured as follows: Section II describes the experimental setup and the method used to obtain the time evolution of pedestal parameters during the ELM cycle. In sections III and IV, the temporal evolution of the electron temperature and density profiles is examined for a series of type I and type III ELMy H-mode discharges. In section V, the radial displacement of the H-mode pedestal during the ELM phase is discussed. The results of ideal MHD stability calculations are shown in section VI. Finally, conclusions are given in section VII.

II. CONDITIONS OF THE EXPERIMENTS

A. Plasma parameters

The results presented in the following sections were obtained from a series of reproducible TCV pulses in lower single-null (SNL) divertor configuration with the ion $\mathbf{B}\times\nabla\mathbf{B}$ drift directed towards the X-point (favourable configuration for the L-H transition). Some of the more important plasma parameters, together with their variation during the discharge periods of interest, are given in table I.

At a plasma current of $I_p = 370$ kA and toroidal magnetic field of $B_\phi = 1.43$ T, the safety factor on axis, q_0, was below unity and sawtooth activity was also observed during the ELMy H-mode phases. Figure 1 shows a representative plasma equilibrium for the sets of type III (blue) and type I (red) H-mode discharges.

With the ion $\mathbf{B}\times\nabla\mathbf{B}$ drift in the favourable direction, transition into H-mode was obtained with ohmic heating only, at a power threshold of $P_{thr} = 330$ kW. For the 3rd harmonic ECH, two gyrotrons at 118 GHz were used, providing a maximum additional heating power of 1 MW. A ray-tracing code TORAY-GA[23] showed that approximately 70% of the injected microwave power was absorbed in the plasma.

Figure 2 shows the classification of ELMs in TCV in the space defined by pedestal density ($n_{e,ped}$) and temperature ($T_{e,ped}$). The subsets of H-mode discharges presented in this paper correspond to cases with pedestal collisionalities $\nu^*_{e,ped} \approx 0.40$ (red) and ≈ 0.75 (blue), where $\nu^*_{e,ped} = 0.1\, Z_{eff} R_0 n_{e,ped} T_{e,ped}^{-2}$ [24] with major radius $R_0\,[m]$, pedestal electron temperature $T_{e,ped}\,[keV]$

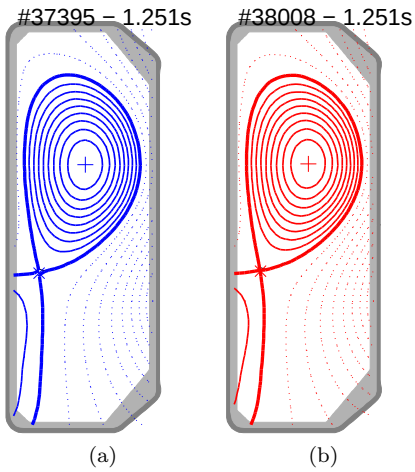

Figure 1. Magnetic flux contours for a representative plasma equilibrium taken from the set of (a) type III (blue) and (b) type I ELMy (red) H-mode discharges. The TCV vacuum vessel with its carbon tiles is shown in grey.

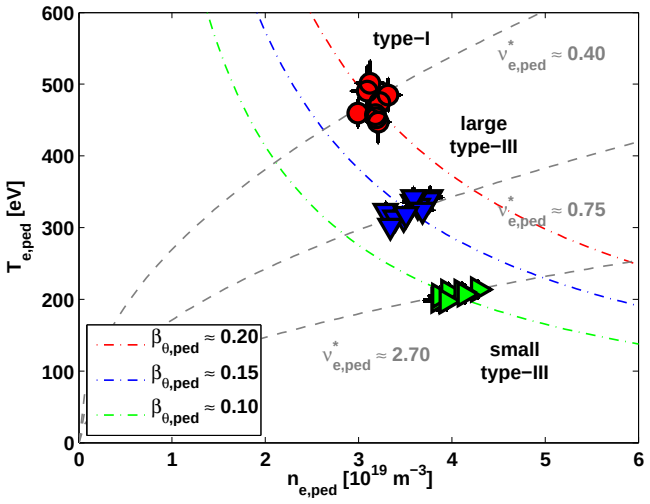

Figure 2. Electron density and temperature at the top of the H-mode pedestal in TCV. Grey dashed lines refer to constant collisionality; colored dash-dotted lines to constant poloidal beta.

and density $n_{e,ped}\,[10^{20} m^{-3}]$. Colored dash-dotted contour lines indicate constant normalized poloidal pressure ($\beta_{\theta,ped}$) and grey dashed mark constant pedestal collisionality ($\nu^*_{e,ped}$), both referring to the values at the top of the pedestal.

A case with higher pedestal collisionality ($\nu^*_{e,ped} \approx 2.7$) has been previously reported[22]; its pedestal parameters are included in Fig. 2 (green) for comparison. These experiments had small type III ELMs at high frequency ($\Delta W_{ELM}/W_{tot} \approx 2\%$, $f_{ELM} \approx 215$ Hz, $\beta_{\theta,ped} \approx 0.08$, $\beta_N \approx 0.4$) and were not well described by ideal MHD due to the high pedestal resistivity.

ELM type	I	III
TCV discharges	$38006 - 38019$	$37391 - 37405$
Plasma current, I_p [kA]	370	370
Total heating power, P_{tot} [MW]	≈ 0.87	≈ 0.40
Safety factor on magnetic axis, q_0	≈ 0.9	≈ 0.9
Safety factor at 95% of normalized poloidal flux radius, q_{95}	≈ 2.3	≈ 2.3
Line-integrated density, $n_{el} = \int n_e(z)\,dz$ $[10^{19}\mathrm{m}^{-2}]$	3.2 ± 0.1	3.6 ± 0.1
Plasma elongation, κ	1.68	1.68
Plasma triangularity, δ	1.45	1.45
Sawtooth frequency, f_{ST} [Hz]	130 ± 30	165 ± 25
ELM frequency, f_{ELM} [Hz]	40 ± 5	75 ± 20
Fractional energy loss per ELM, $\frac{\Delta W_{ELM}}{W_{tot}}$ [%]	20 ± 3	8 ± 2
Fractional electron energy loss per ELM, $\frac{\Delta W_{e,ELM}}{W_{e,tot}}$ [%]	36 ± 4	14 ± 2
Effective charge, Z_{eff}	≈ 2.5	≈ 3.5
Pedestal collisionality, $\nu^*_{e,ped}$	≈ 0.40	≈ 0.75
Normalized pedestal poloidal pressure, $\beta_{\theta,ped}$	≈ 0.20	≈ 0.15
Normalized toroidal pressure, β_N	≈ 1.05	≈ 0.55
Energy confinement enhancement factor, $H_{IPB98(y,2)}$	≈ 0.95	≈ 0.65

Table I. Some plasma parameters of the series of TCV pulses with ELMs of type I and type III, taken from the quasi-steady state ELMy H-mode phase. The fractional energy loss per ELM, $\Delta W_{ELM}/W_{tot}$, was obtained from the diamagnetic loop diagnostic(DML); the factional electron energy loss per ELM, $\Delta W_{e,ELM}/W_{e,tot}$, from Thomson scattering.

B. Measurements and data analysis

The spatial profiles of electron temperature (T_e) and density (n_e) were measured by the TCV Thomson scattering system along a laser beam path that traverses the plasma vertically close to the magnetic axis[25]. For the selected plasma configuration, the pedestal region is covered by 9 observation volumes with a vertical extension of $\Delta z = 12$ mm. When the profiles are mapped onto radial coordinates in the equatorial plane of the plasma, the effective spatial resolution is better than 5 mm as a result of the high poloidal flux expansion.

The 3 independent laser beams are combined into a narrow fan and scattered light is collected by 2 wide-angle camera lenses that image the observation volumes onto fiber-optic bundles. In the image plane, the scattering volumes attributed to the individual laser beams appear superposed. Therefore, alternate triggering of the lasers, which operate at a fixed repetition rate of 20 Hz, can be used to increase the effective sampling rate.

The data was collected from selected time windows within each discharge to ensure that the variation of plasma parameters was maintained within narrow limits. An overview of relevant parameters and of their variation are given in table I. Criteria for selection of the time window were constant electron temperature (T_e), line-integrated electron density (n_{el}), plasma current (I_p), safety factor (q_{95}), plasma shape and X-point location. This is a prerequisite for the application of the method of random sampling and coherent averaging that was used to reconstruct the time evolution of T_e and n_e profiles across the ELM cycle. For this purpose, the measurements recorded during quasi-stationary ELMy H-mode phases from several discharges were grouped according to their time separation from the closest ELM event. The data sets within each group were modeled by an analytical function to obtain time-averaged profiles at an effective sampling rate on the ms-time scale. The evolution of profile parameters during a typical ELM cycle was thus resolved in spite of the low repetition of the Nd:YAG lasers.

During the H-mode period, the profile in the pedestal region is well represented by a modified tanh function with five free parameters[18], which may directly be associated with the quantities of interest, namely pedestal height, pedestal width and maximum gradient. This method has already been successfully applied in a previous study[22] and by other authors[26,27].

Although the statistical uncertainties in the fitting parameters are substantially reduced using coherent averaging, some systematic errors cannot be excluded. As the Thomson scattering data is mapped onto flux surfaces and thus onto the equatorial midplane of the plasma, inaccuracies of the equilibrium reconstruction will affect the results. In particular, the location of the separatrix has an uncertainty of the order of a few mm. The relative spacing of the data points that is most relevant in the evaluation of the parameter gradients, should, however, remain accurate. The spatial sampling interval of the measurements sets a lower limit to the resolvable pedestal width. In the presented cases, considerable smoothing effects are expected for pedestal widths below 4 mm. For comparison, usual pressure pedestal widths in ELMy H-mode plasmas in TCV are around 10 mm, which is close

to the ion Larmor radius in the edge.

Ion temperature (T_i) profiles were only measured for a subset of discharges using charge-exchange recombination spectroscopy (CXRS) with a diagnostic neutral beam injected along the equatorial plane of TCV. Spatially resolved measurements of the ion temperature of the carbon impurity ions (dominant TCV impurity) were obtained from analysis of the $C-VI$ line[28]. An integration time of 30 to 50 ms (imposed by signal-to-noise requirements) was required so that, averaging over more than a full ELM cycle, transient features near the edge perturb the results. No attempt was thus made to extract an ion temperature gradient in the pedestal region during the ELM cycle. Nevertheless, reliable measurements of T_i at the top of the pedestal have been obtained and confirm that $T_i \approx T_e$ at this location.

III. TYPE I ELMS

An example of an H-mode phase with type I ELMs (TCV-#38006) is shown in Figs. 3(a) and 3(b), representing the traces of D_α emission from the divertor region, line-integrated electron density (n_{el}) and normalized soft X-ray emission (soft-X) along central and off-axis chords. During the quasi-stationary phase, shown in grey, the ELM frequency was about 40 Hz and the relative energy loss per ELM, as measured by the diamagnetic loop, reached values near 20%. This rather large loss is due to a drop in T_e over the full plasma cross section, as will be shown later.

Indications for a global drop in plasma energy content can already be seen on the traces of n_{el} and soft X-ray emissivity, Fig. 3(c), obtained by coherent averaging with respect to the ELM event identified by the spike in the D_α intensity. The rapid drop of the soft X-ray intensity at the center coincident with the ELM is typical for these conditions. It should be noted that sawtooth (ST) activity is also present during these phases, but at a frequency substantially higher than the ELM. A coincidence of the ELM crash with a sawtooth cannot be excluded but could not be clearly established.

Fig. 4(a)(i)-(iii) show the time evolution of the pedestal parameters (max. gradient (∇), width (Δ) and height) for T_e obtained from profile fitting to the data sets organized in time-bins. Figs. 4(a)(iv)-(v) show central and volume averaged electron termperature ($T_e(0)$ and $\langle T_e \rangle_{vol}$). Fig. 4(a)(vi) shows the probability for a sawtooth crash at a given time during the ELM cycle. It is obtained by counting the number of ST events N within a window of $\Delta t = 0.5$ ms for each time delay $t_i - t_{ELM}$ and normalising to the total number of ST events : $P_{ST}(t) = N(t, \Delta t)/\sum N$. The times before and after the ELM event are treated separately.

Spatial profiles of T_e in the pedestal region (radial coordinate along the midplane) and over the full normalized radius (ρ_ψ) are given in Fig. 5 (a) for representative time steps during the ELM cycle. The same procedure was applied to the data sets of electron density and pressure (results shown in Figs. 4 and 5, (b) and (c) respectively).

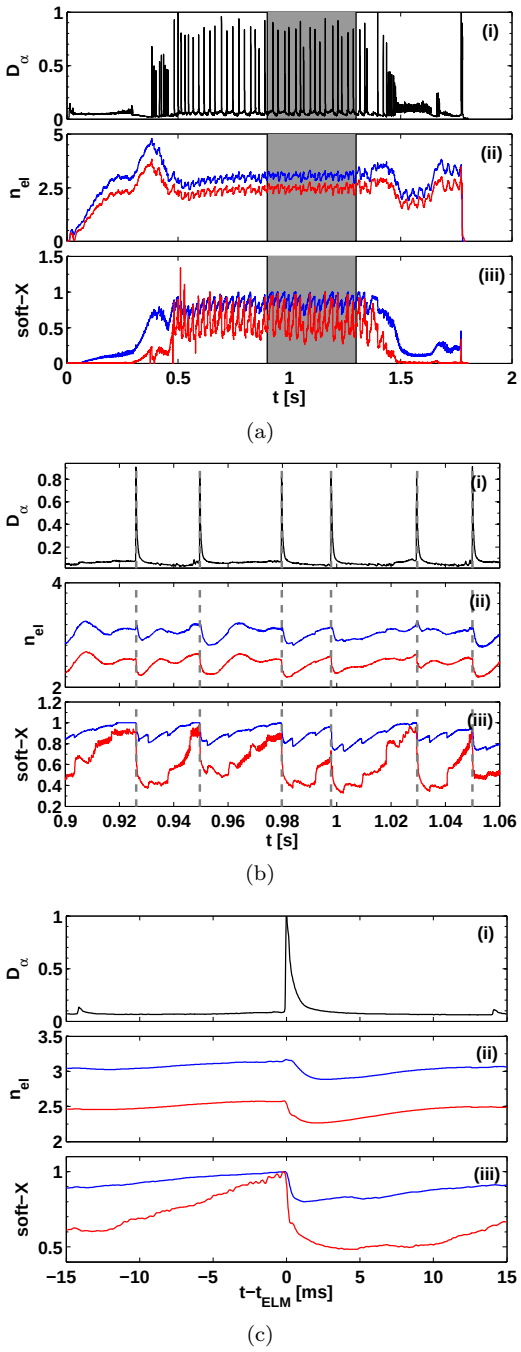

Figure 3. type I ELMy H-mode: Traces of the (i) normalized D_α emission, (ii) line-integrated density (n_{el} $[10^{19}$ m$^{-2}]$) and (iii) normalized soft X-ray emission (soft-X) from viewing lines looking at the plasma center (blue) and the LFS-edge (red). (a) shows the traces for the full discharge length and (b) for a selected time window during the quasi-steady state ELMy H-mode phase. Coherent averaging was applied to the data in the grey-shaded region of (a) and the results are shown in (c).

Spatial profiles of T_e in the pedestal region (radial co-

ordinate along the midplane) and over the full normalized radius (ρ_ψ) are given in Fig. 5 (a) for representative time steps during the ELM cycle. The same procedure was applied to the data sets of electron density and pressure (results shown in Figs. 4 and 5, (b) and (c) respectively).

Although the analysis encompasses many ELM events, coherent averaging reveals some clear tendencies: For T_e, we observe a gradual increase in the pedestal height ($T_{e,ped}$) and the strongest gradient during the time interval 5 to 10 ms before the ELM event (ELM period about 25 ms). During this phase, $T_e(0)$ and $\langle T_e \rangle_{vol}$ remain nearly constant. At the ELM, a rapid decrease (collapse) is seen, not only for $T_{e,ped}$ ($0.65 \rightarrow 0.46$ keV) and $\nabla(T_e)$ ($95 \rightarrow 48$ keV/m), but also for $T_e(0)$ ($2.5 \rightarrow 2.0$ keV) and $\langle T_e \rangle_{vol}$ ($1.3 \rightarrow 1.0$ keV). Clearly, the ELM-induced collapse is not restricted to an edge region, but affects the whole plasma volume (see Figs. 4(a)(iv)-(v) and Fig. 5(a)), which explains the rather high relative energy loss per ELM of 36% for the electron population (20% according to global measurements by a diamagnetic loop).

The post-ELM recovery phase is characterized by a gradual build-up of $T_e(0)$ and $\langle T_e \rangle_{vol}$, which requires about 1/2 of the period of the ELM cycle (i.e. ≥ 10 ms). A significant rise of $T_{e,ped}$ and $\nabla(T_e)$ only commences during the second part of the cycle.

The evolution of the density profile is different. There is no substantial rise in $n_{e,ped}$ nor $\nabla(n_e)$ during the interval of 5 to 10 ms before the ELM event. However, when $T_e(0)$ has reached its maximum, $n_e(0)$ tends to decrease, which is interpreted as a sign of density pump-out[29].

At the time of the ELM event, the pedestal parameters ($n_{e,ped}$, $\nabla(n_e)$) show the signature of a collapse and even $\langle n_e \rangle_{vol}$ decreases, which indicates a significant loss of particles from the plasma. The transient increase in $n_e(0)$ signals a temporary profile peaking, also visible on the profiles shown in Fig. 5 (b), bottom. The density profiles appear to already reach their pre-ELM values after 5 to 7 ms.

The evolution of the electron pressure profiles reflects the combined effects on T_e and n_e. The ELM crash is characterized by a drop in $p_{e,ped}$ from 3.8 to 2.2 kPa and of $\nabla(p_e)$ from 450 to 175 kPa/m. The central pressure $p_e(0)$ and the volume averaged pressure $\langle p_e \rangle_{vol}$ decrease by 20% and 35% respectively. This explains the large value of the relative energy loss per ELM ($\sim 20\%$).

Although pedestal pressure and the steepness of the pressure gradient near the edge rise during the 5 ms before the ELM, it is not clear whether the ELM trigger is governed by a threshold. The analysis of the MHD stability limits, results are presented in Sec. VI, elucidate this point. There is also no evidence that ST activity plays a role for triggering of these ELMs. A different observation was made in case of type III ELMs, as will be shown in Sec. IV.

IV. TYPE III ELMS

The second set of TCV ELMy H-mode discharges, which are ohmically heated only, exhibits type III ELMs with a relatively low ELM frequency of around 75 Hz, large relative ELM power loss of about 8% and a correlation between ST activity in the pre-ELM phase and the ELM event. The case of small ELMs of type III (ELM frequency ~ 215 Hz and relative energy loss of $\sim 2\%$), observed in TCV plasmas at higher densities and ohmic heating only, was reported in an earlier publication[22]. At higher pedestal collisionality, resistive effects become important and a stability analysis, based on ideal MHD, is questionable and are, therefore, not included herein.

Fig. 6(a) shows traces of the normalized D_α emission, n_{el} and normalized soft X-ray for a representative discharge (TCV-#37395), and 6(b) for a selected time interval taken from the stationary ELMy phase. The coherently averaged traces, Fig. 6(c), show only a small drop in line-integrated density by less than 5% in the core and edge at the ELM event. The soft X-ray emission drops at the edge at the ELM onset and shows a clear sign of ST activity shortly (~ 1 ms) before the ELM. This is not observed for type I ELMy H-mode in TCV as discussed in Sec. III.

Although the data presented in Fig. 7 is extracted from more than 10 discharges, i.e. around 7 s of stationary ELMy phase, a clear signature of ST activity is visible on $T_e(0)$, Fig. 7(a)(iv). Despite the coherent data resampling and averaging, 2 ST crashes are clearly observed during one full ELM cycle (~ 13 ms) indicating a synchronization between ELM and ST activity. One sawtooth precedes the ELM by around $1-2$ ms, not only provoking a drop in $T_e(0)$ and $n_e(0)$ of about 5%, but also affecting the T_e and n_e pedestals by decreasing their widths, Figs. 7(a)(ii) and 7(b)(ii). The electron pressure dynamics, Fig. 7(c), shows clearly that the pre-ELM sawtooth affects the pedestal such that the pedestal gradient raises until an ELM is destabilized. The nature of the destabilized mode will be discussed in more detail in Sec. VI.

Similar observations have been reported from other tokamaks (JET[30], AUG[31], JT-60[32], Textor[33]), where the presence of instabilities driven by energetic particles, such as caused by ST and fishbones, has been investigated as potential precursor for ELMs. For example, in AUG it was found that there is a coupling of the fishbone instability ($m > 1$ and $n \sim 1$) with type I ELMs[31] during high-β discharges. In JET's high-β discharges ($\beta_N > 0.5$), ELMs were found to couple to sawteeth[30]. However, such coupling would appear more likely for type I ELMs presented in Sec. III, where $\beta_N \approx 1.05$ is twice the value of that of the typical type III ELMy H-mode in TCV. Further studies are needed to clarify this issue.

After a rapid drop in $\nabla(p_e)$ ($200 \rightarrow 100$ kPa/m^3) at the ELM event, which is dominated by the drop in ∇n_e, the pedestal gradient recovers within around a millisecond. The central electron pressure increases by about 10%,

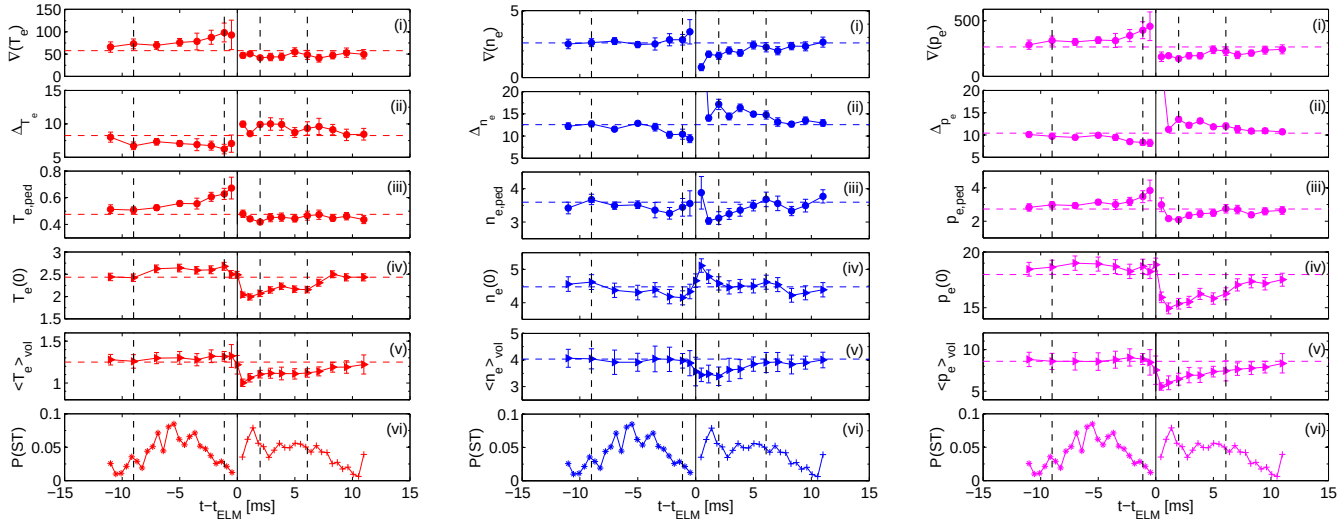

Figure 4. Temporal evolution of (a) electron temperature, (b) density and (c) pressure during cycles with type I ELMs: Shown are (i) pedestal radial gradients ($\nabla(T_e)$, $\nabla(n_e)$, $\nabla(p_e)$ in keV/m, 10^{21}m^{-4}, kPa/m), (ii) pedestal widths (Δ_{T_e}, Δ_{n_e}, Δ_{p_e} in mm), (iii) pedestal heights ($T_{e,ped}$, $n_{e,ped}$, $p_{e,ped}$ in keV, 10^{19}m^{-3}, kPa), (iv) central values ($T_e(0)$, $n_e(0)$, $p_e(0)$ in keV, 10^{19}m^{-3}, kPa), (v) volume-integrated values ($\langle T_e\rangle_{vol}$, $\langle n_e\rangle_{vol}$, $\langle p_e\rangle_{vol}$ in keV, 10^{19}/m^3, kPa) and (vi) probability of ST activity $P(ST)$ normalized to unity in the pre- and post-ELM phases. Black dashed lines represent the times for which the profiles are shown in Fig. 5.

mainly due to a density peaking (compare with bottom Fig. 8(b)), whilst the volume-integrated pressure drops by about 15%.

During the post-ELM phase, the recovery of pedestal and global parameters show two distinct phases, again influenced by ST activity. In the first phase, until $\sim$ 3.5 ms, pedestal quantities and $\langle p_e\rangle_{vol}$ gradually rebuild, although the pre-ELM value of $p_{e,ped}$ and $\langle p_e\rangle_{vol}$ is only reached in the longer second phase ($\sim$ 9 ms).

In general we notice that the ELM cycle affects more strongly the n_e profile (Fig. 8), in contrast to the case of type I ELMs (Fig. 5).

V. DISPLACEMENT OF THE EDGE PEDESTAL DURING THE ELM CYCLE

The analysis of the pedestal tanh fit results from Sec. III and IV reveals a radial displacement of the edge pedestal towards the plasma center in the presence of strong ECH and hence type I ELMs. Fig. 9 shows the radial positions (R_0) of the electron temperature (red), density (blue) and pressure (magenta) pedestal center, i.e. the location of largest gradient in the tanh fit, with respect to the position of the separatrix (R_{LCFS}) normalized by the pedestal width (Δ) for the sets of type I and type III ELMy H-mode data analyzed above. The relative pedestal position $R_0 - R_{LCFS}$ is normalized by Δ to avoid biasing by a change of the pedestal width during the ELM cycle. Colored dashed horizontal lines correspond to the value taken from mid-time between ELMs. A normalized distance of 0.2 corresponds approximately to a difference of $\Delta\rho = 10^{-2}$ in normalized poloidal flux radius.

The results show clear signs of pedestal displacement from the separatrix inwards throughout the whole pre-ELM phase in the case of *type I ELMs*. The magnitude of this movement increases with heating power[12]. The displacement of the pedestal is more pronounced on the T_e profile, Fig. 9(a)(i), whereas the radial position of the n_e pedestal only changes shortly ($\sim$ 5 ms) before the ELM. The radial position of the pressure pedestal at mid-time in the ELM cycle is $\rho_0 \approx 0.990$. During the pre-ELM pedestal build-up, the radial position moves gradually inwards. Shortly before the ELM is observed on the D_α intensity, the position is $\rho_0 \approx 0.981$. The inward displacement of the pedestal has direct consequences on the MHD stability limits of the pedestal, as will be described in more detail in Sec. VI.

In contrast, for the case of *type III ELMs*, the pedestal radial position is nearly constant throughout the pre-ELM phase. Note that the value of the radial position of the p_e profile at mid-time in the ELM cycle, $\rho_0 \approx 0.984$, is farther inwards than for the case of type I ELMs.

Errors in the absolute and relative values of the pedestal position $R_0 - R_{LCFS}$ may occur for several reasons: (1) The exact determination of the LCFS is non-trivial and only accurate to within a few millimeters. For the set of discharges presented in this study, the equilibrium reconstructions were verified and, if necessary, corrected to match the Thomson profiles from the upper and lower parts of the plasma. The maximum correction

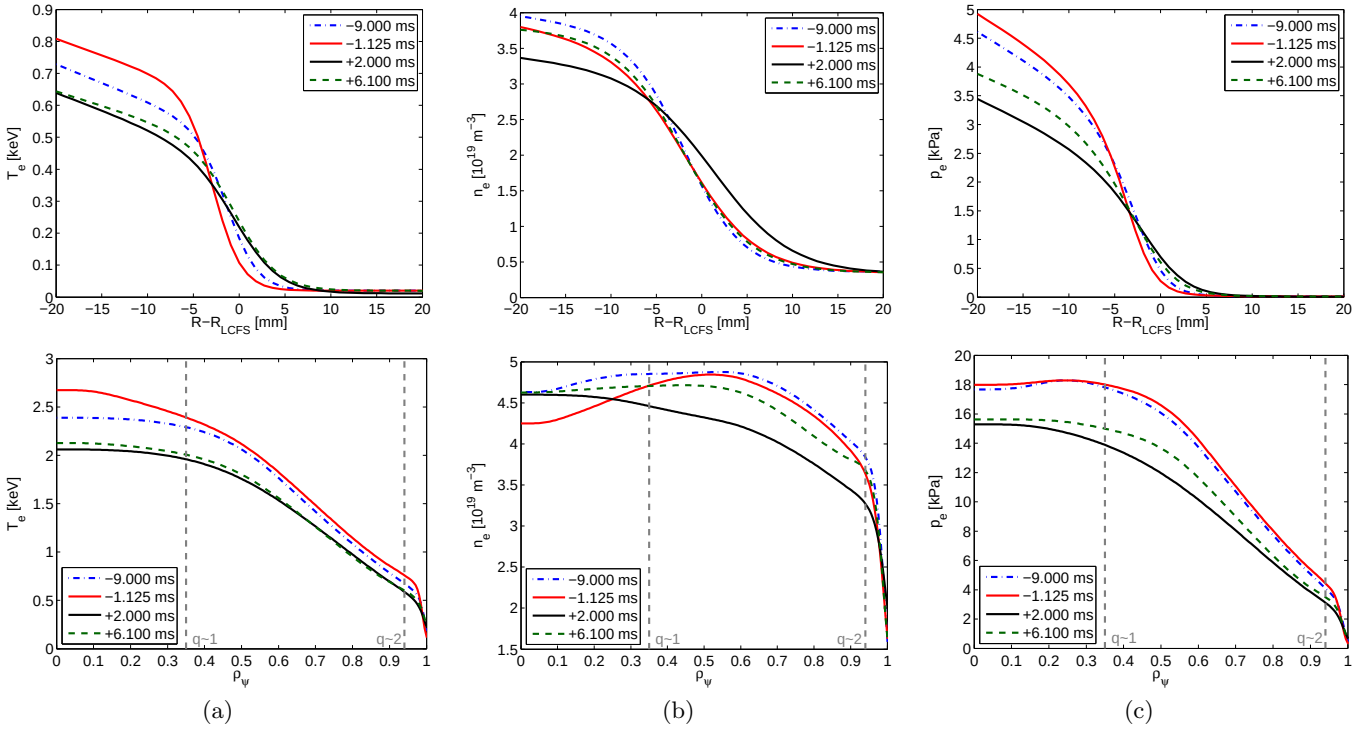

Figure 5. Electron temperature, (b) density and (c) pressure as function of the normalized relative radius, $R - R_{LCFS}$, and normalized poloidal flux radius, ρ_ψ. Pedestal profiles are shown in the upper, complete profiles in the lower line. Solid lines represent the pre- and post-ELM profile, dashed colored lines show profiles from the ELM cycle at selected times. The position of the rational q-surfaces is indicated by grey dashed vertical lines.

applied on the vertical plasma position was < 5 mm, i.e. $\delta\left[\left(R_0 - R_{LCFS}\right)/\Delta\right] < 0.1$. (2) The effect of the bootstrap current density is not taken into account in the LIUQE[34] equilibrium reconstruction. For a high and steep pedestal, the bootstrap current fraction becomes important. The additional edge current increases the differential change in poloidal flux, i.e. the magnitude of radial pedestal movement would be presumably larger than indicated before. (3) The equilibrium reconstruction may not precisely reproduce the Shafranov shift across the ELM cycle, inducing uncertainties in mapping from the vertical observation line to the plasma midplane. Systematic errors in the radial position would be observed for both, electron and density, pedestals whereas, in our case, the radial displacement differs between the T_e and n_e pedestals. (4) Analysis of the time-averaged profiles will average out statistical errors, but may introduce other uncertainties. In particular, irreproducible events will always pollute the data set.

Recent measurements of the pedestal electron temperature and density in AUG[11] and DIII-D[35] for type I ELMs revealed similar trends of the temporal pedestal evolution. At least two different theoretical models exist that describe time-dependent pedestal expansion[36,37]. Both predict that the pedestal should expand inwards and are based on the hypothesis that pedestal transport coefficients are reduced by $\mathbf{E} \times \mathbf{B}$ shear, which was successfully modeled with the ASTRA code for a DIII-D discharge[38].

VI. IDENTIFICATION OF THE PEDESTAL PRESSURE GRADIENT LIMIT BY IDEAL MHD

The ideal MHD code KINX[21] was developed to investigate the stability limits of pressure and current driven modes in the plasma. In particular, it is well suited to deal with cases of high magnetic shear and high safety factor q near the edge, which are typical for plasmas with X-point and separatrix. Therefore, it has been used for this study in combination with the codes CHEASE[39] and CAXE[40] that describe the fixed-boundary MHD equilibrium.

It should be noted that KINX solves the equations of ideal MHD without any assumptions on the radial or poloidal localisation of the modes. Therefore, MHD modes over a wide range of toroidal mode numbers n are included in the analysis. They are driven by the combined effect of pressure gradient and edge current density. We refer to them as kink-ballooning modes, whereas in the past a distinction between current-driven kink modes and pressure-driven ballooning modes was often made.

Starting with the prescribed plasma boundary and with pressure and current density profiles given as input, the suite of equilibrium and stability codes produces a stability map in the space of normalized pressure gradi-

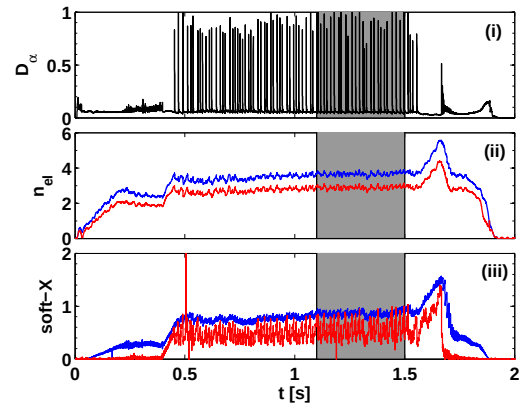

(a)

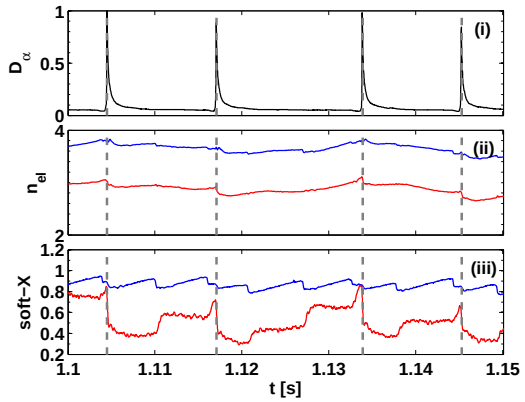

(b)

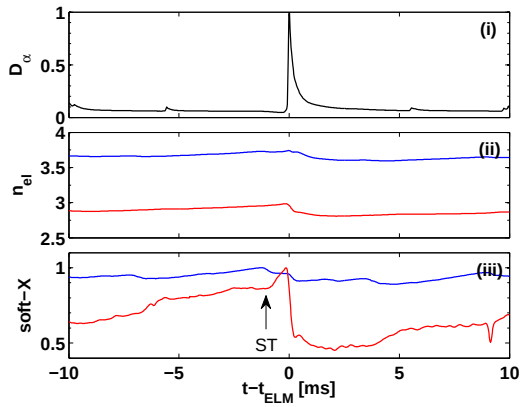

(c)

Figure 6. type III ELMy H-mode: Traces of the (i) normalized D_α emission, (ii) line-integrated density (n_{el}) and (iii) soft X-ray emission (soft-X) from viewing lines looking at the plasma center (blue) and the LFS-edge (red). (a) shows the traces for the full discharge length and (b) for a selected time interval with dashed grey vertical lines indicating the time of the ELM onset. Coherent averaging was applied on the data in the grey-shaded region and the results are shown in (c).

ent and parallel current density in the pedestal region. This diagram will reveal the unstable regions and may serve to identify the modes that are responsible for the edge stability limitations.

For the present study, the shape of the pressure profiles is obtained from experimental data provided by Thomson scattering measurements and additional information from charge-exchange recombination spectroscopy (CXRS) to confirm the assumption of $T_i = T_e$ in the edge region. The effective ion charge has been fixed to the values given in Table I. A first approximation of the current density profiles is obtained from equilibrium reconstruction (LIUQE). However, these profiles are not precise enough in the edge region, where the pressure gradient drives a substantial amount of bootstrap current. This contribution is calculated separately from the experimental pressure profiles using analytical expressions derived by Sauter[41] on the basis of a Fokker-Planck model. After adding this component, the resulting current density profile is rescaled to match the total plasma current.

The stability maps, Figs. 10 and 11, are presented as function of the normalized parallel current density $J_{//}/\langle J\rangle$ and normalized pressure gradient α at the edge. $J_{//} = \langle \mathbf{j}\cdot\mathbf{B}\rangle/\langle|\mathbf{B}|\rangle$ is taken at the position where the pressure gradient is maximal, $\langle J\rangle = I_p/S_p$ is the total plasma current normalized to the plasma cross sectional area. For the normalized pressure gradient, we use the definition $\alpha \equiv \mu_0\,(dp/d\psi)\,(dV/d\psi)\,\sqrt{V/\,(2\pi^2 R)}/2\pi^2$ [18] taken at the point of maximum pressure gradient in the pedestal, where p is the total pressure, V is the plasma volume, R the major radius and ψ the poloidal flux. More information about relevant pedestal parameters is given in Tab. II.

To cover the parameter range in α and $J_{//}/\langle J\rangle$, the pressure and current density profiles in the edge region are scaled and a new equilibrium is calculated for each step, keeping the the total current and the shape of the plasma boundary constant. In this way, the stability conditions are obtained over a rather fine grid in the parameter space, sufficient to trace the stability limits for modes of various toroidal mode numbers by interpolation.

It is worth noting that in general these stability diagrams are calculated keeping the position of the maximum pressure gradient and the maximum in the bootstrap current contribution fixed and varying only their magnitude. Systematic studies[17] have shown that a variation of the location and/or the width of the gradient zone will affect the growth rates of modes of different n and shift the effective stability boundaries and the most unstable mode numbers. As will be shown later (see Figs. 10 and 11), a single stability diagram may not be sufficient to discuss the dynamic behaviour during the ELM cycle.

The stability boundary for ideal ballooning modes with $n \to \infty$ is obtained from CHEASE for a set of poloidal flux surfaces. In the diagrams, the limit for destabilizing any flux surface is shown as solid red line. The stable region is found above and to the left of this boundary. The growth rates of the external kink-ballooning modes with finite toroidal mode number n were computed by KINX and extrapolated to infinite grid size assuming

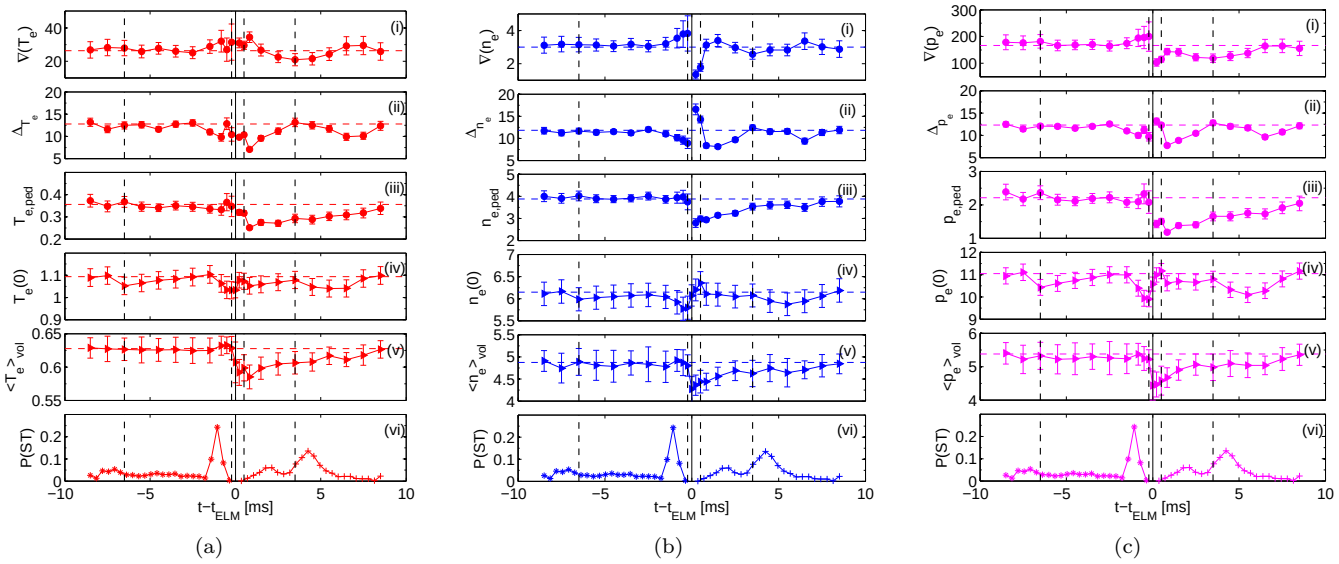

Figure 7. Temporal evolution of (a) electron temperature, (b) density and (c) pressure during cycles with type III ELMs: Shown are (i) pedestal radial gradients ($\nabla(T_e)$, $\nabla(n_e)$, $\nabla(p_e)$ in keV/m, $10^{21}\mathrm{m}^{-4}$, kPa/m), (ii) pedestal widths (Δ_{T_e}, Δ_{n_e}, Δ_{p_e} in mm), (iii) pedestal heights ($T_{e,ped}$, $n_{e,ped}$, $p_{e,ped}$ in keV, $10^{19}\mathrm{m}^{-3}$, kPa), (iv) central values ($T_e(0)$, $n_e(0)$, $p_e(0)$ in keV, $10^{19}\mathrm{m}^{-3}$, kPa), (v) volume-integrated values ($\langle T_e\rangle_{vol}$, $\langle n_e\rangle_{vol}$, $\langle p_e\rangle_{vol}$ in keV, $10^{19}/\mathrm{m}^3$, kPa) and (vi) probability of ST activity $P(ST)$ normalized to unity in the pre and post-ELM phases. Black dashed lines represent the relative times for which the profiles are shown in Fig. 8.

ELM type	I	III
TCV discharge	38008	37395
Position of maximum edge pressure gradient in normalized radius, ρ_0	0.990 (0.981)	0.985
Pedestal full width at half maximum (FWHM) in normalized radius, Δ_ρ	0.025 (0.025)	0.022
Edge current ratio, $j_{\|\|}(edge)/j_{\|\|}(\rho_0)$	0.65 (0.28)	0.47
Edge pressure gradient ratio, $p'(edge)/p'(\rho_0)$	0.73 (0.34)	0.54

Table II. The pedestal location ρ_0 is given in normalized poloidal flux radius $\sqrt{\psi/\psi_0}$, its width Δ_ρ in the same coordinate. The ratio between edge and maximum pressure gradient $p'(edge)/p'(\rho_0)$ and the ratio between edge and maximum current density $j_{||}(edge)/j_{||}(\rho_0)$ influence the stability limits of ballooning and external kink modes. Values in parenthesis correspond to the pre-ELM equilibrium, where radial displacement of the pedestal is taken into account (see Sec. V).

$(N_\psi \times N_\chi)^{-1}$ convergence, where N_ψ and N_χ are the number of radial and poloidal grid points. The stability limits for finite-n kink-ballooning modes are presented as colored lines together with the respective n. With respect to these modes, the stable area lies below and to the left of these limits. Collisionless bootstrap current and shear reversal limit are shown as dash-dotted and dashed lines.

Due to diamagnetic effects in the pedestal region[15,42], modes with high toroidal mode numbers are expected to be stabilized. The maximum unstable n is estimated by $n_{max} \cong (\epsilon L_p)\,/\,(q\rho_i)$ assuming the diamagnetic drift frequency (ω_{*pi}) to be unchanged throughout the pedestal. Here, ϵ is the inverse aspect ratio, $L_p = |d(\ln p_i)/dr|^{-1}$ the characteristic ion pressure gradient scale length, ρ_i the ion Larmor radius and q the safety factor. For the computation of n_{max}, $R_0/L_{pi} = 100$ (R_0 major radius), $n_e = 3 \times 10^{19}\mathrm{m}^{-2}$ and $T_i = T_e$ were used. In general we find that higher mode numbers ($n \geq 20$) are stabilized by diamagnetic effects, including the infinite-n ideal ballooning mode. However, a more precise representation of the diamagnetic stabilization by the EPED1.6 code shows a stronger stabilization at low n and significantly weaker stabilization at high n, which is particularly important in smaller tokamaks where ω_*/ν_A (Alvén frequency ν_A) tends to be relatively large[43].

The point in $j-\alpha$ space time-averaged over the ELM period is labeled as **A** and includes the bootstrap current based on the experimental profiles and assumptions mentioned above. The equilibrium is consistent including all corrections stated above, however, the separatrix shape is taken from the LIUQE reconstruction and does, thus, not include the bootstrap current. The horizontal error bar accounts for the uncertainty in the total pressure gradient. The vertical error bar takes into account

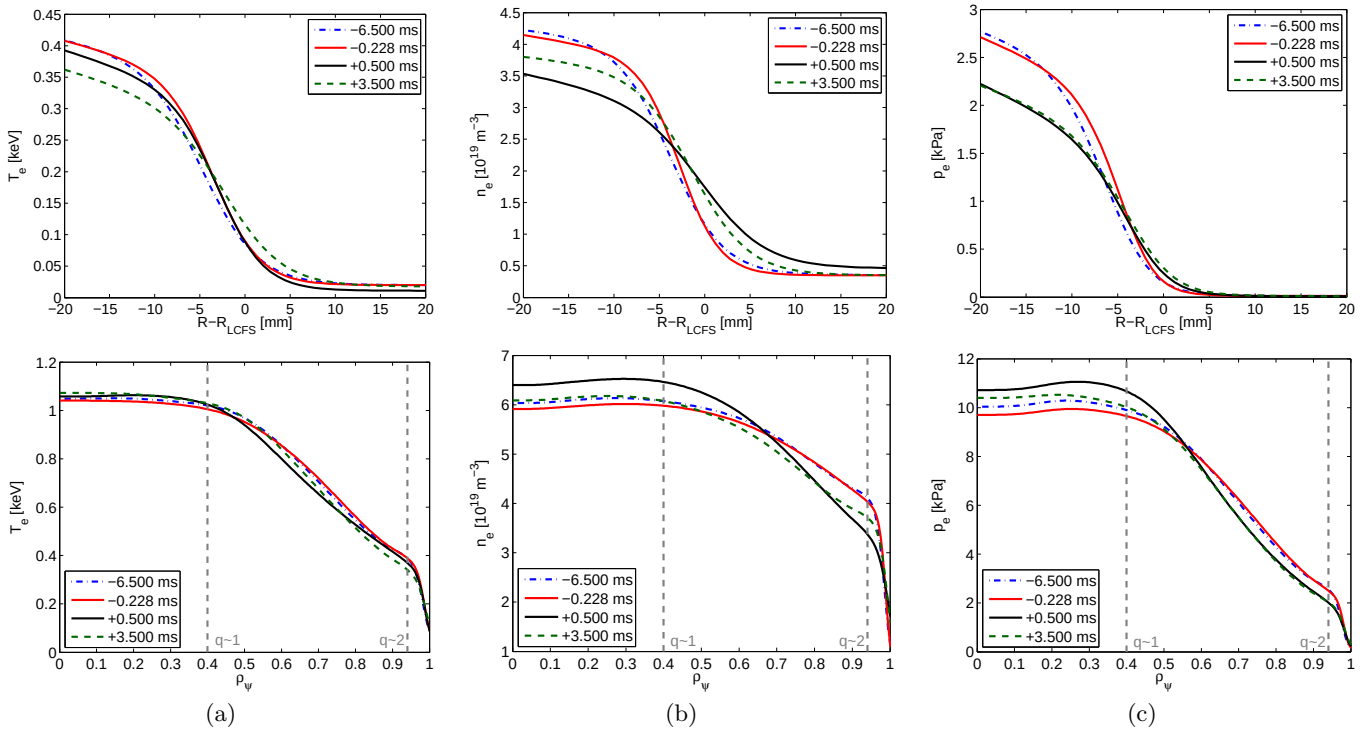

Figure 8. Profiles of (a) electron temperature, (b) density and (c) pressure in the pedestal region (top) and for the whole cross section (bottom). Pedestal profiles are given in relative radial coordinates in the plasma equatorial plane (R_{LCFS} = separatrix), the other profiles are shown in normalized poloidal flux coordinates ρ_ψ. Solid lines represent the pre- and post-ELM profile, dashed lines show profiles from the ELM cycle at selected times. The position of the rational q-surfaces is indicated by vertical dashed grey lines.

the uncertainty in the bootstrap current. The points **B** and **C** represent the conditions in the pre-ELM pedestal evolution for selected times shortly before an ELM. The point **D** is computed from profiles in the post-ELM phase around $0.5 - 1.5$ ms after the ELM crash. In this case, the current density profile is taken from the last pre-ELM profile under the assumption of negligible current diffusion during a total time delay of less than ~ 3 ms during the ELM crash.

A. Type I ELMs

In the frame of ideal MHD, high pedestal pressure gradients and large bootstrap current densities close to the separatrix lead to the destabilization of external kink-ballooning modes, which are generally associated with ELMs. However, ELM triggering does not appear to be a simple threshold effect. Operation near a stability limit is a necessary, but not a sufficient, condition for their appearance. Some ELMs were directly triggered when the pressure gradient attained a critical value imposed by ideal MHD[5,44]. However, in other cases it has been observed that the pedestal remains at the pressure limit for several milliseconds before an ELM occurs[31,35].

Fig. 10(a) shows the stability map for a type I ELMy H-mode discharge. The point **A**, which refers to a time-averaged pressure profile, is still in a region that is marginally stable to infinite-n ballooning modes. The data from the pre-ELM phase yield the points **B** ($t - t_{ELM} = -5$ ms) and **C** ($t - t_{ELM} = -1.5$ ms). We observe that pedestal conditions gradually evolve in such a way that they approach the low- or intermediate-n kink-ballooning mode stability limit. Eventually, an ELM occurs and the pedestal relaxes. Point **D** ($t - t_{ELM} = 1.5$ ms) represents the pedestal shortly after the ELM crash assuming negligible current diffusion during the ELM. After the ELM crash, the normalized pressure α is close to the inter-ELM value.

In a recent publication, Groebner et al.[45] showed the evolution of normalized pressure gradient and edge current during cycles with type I ELMs for a reference shot in DIII-D. The general trends seen on a stability map are fairly similar to our observations both with respect to the high-n ideal ballooning and the kink-ballooning limits.

If we want to use the stability diagrams to trace the dynamic process of the pressure profile evolution, we need to take into account that it is not described by simply rescaling the amplitude of the p'-profile. Fig. 10(b) shows a comparison of the stability diagrams based on the experimental profiles of points **A** (dashed lines) and **C** (solid lines). By accounting for the displacement of the pedestal towards the plasma center in the pre-ELM phase (point **C**), as was presented in Sec. V, stability limits of current-

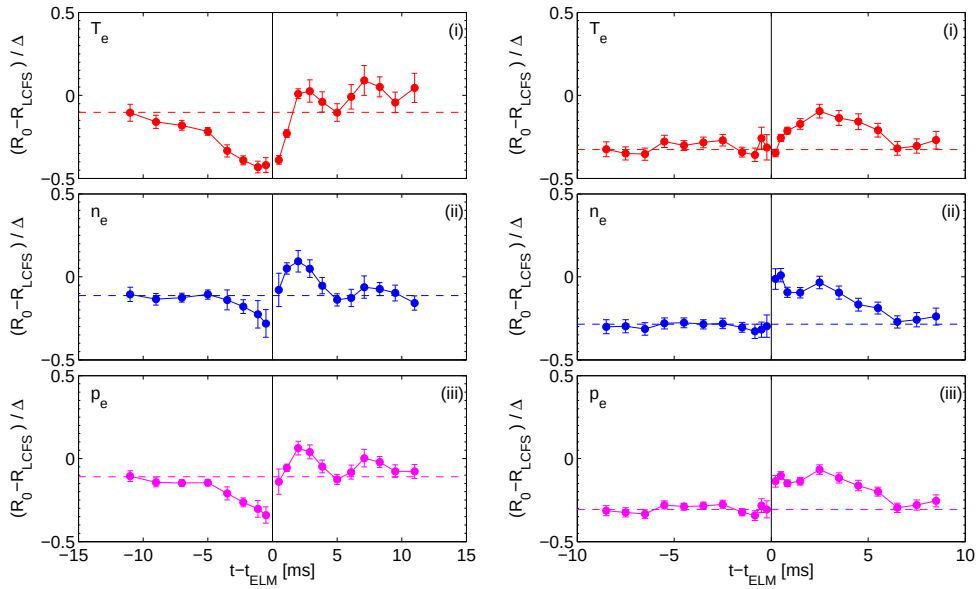

(a) type I ELMs (b) type III ELMs

Figure 9. Edge pedestal displacement during the ELM cycle: Shown are the positions of the pedestal center of electron temperature (red), density (blue) and pressure (magenta) pedestal during a (a) type I and (b) type III ELM cycle.

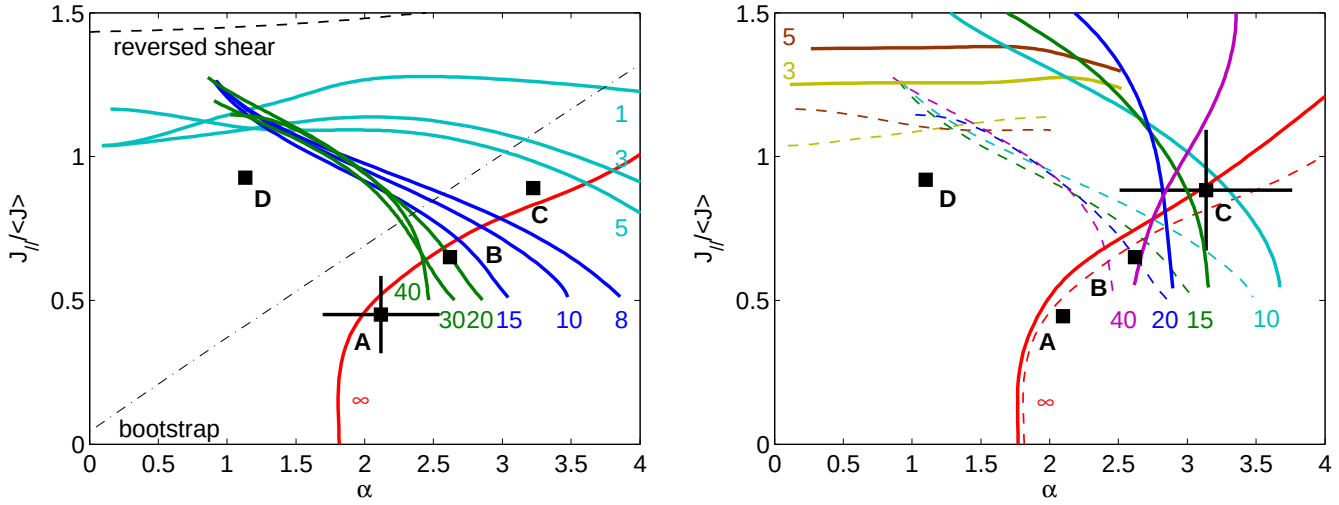

(a) (b)

Figure 10. Ideal MHD stability maps for a type I ELMy H-mode discharge based on (a) the profile from a time-average over the ELM period, i.e. without effects of pedestal displacement, and (b) on the pre-ELM profile with radially displaced pedestal: The point A represents the ELM period time-averaged profile and B, C & D refer to the relative times $t - t_{ELM} = \{-5.0, -1.0, +1.5\}$ ms in the ELM cycle. The stability limits from (a) are replotted in (b) as thin dashed lines for comparison purpose.

driven modes shift to higher α's, whereas the ballooning limit is decreased. The improvement in pedestal stability is due to a decrease of bootstrap current density close to the separatrix stabilizing current-driven external kink modes. Although less pronounced, the increase of the current density further inside the plasma decreases the shear ($s(\rho_0) = 2.0(2.8)$ and $q(\rho_0) = 2.7(2.8)$ for points C and A with $\rho_0 = 0.981(0.990)$) destabilizing the pressure-driven ballooning modes.

Experimental observations and predictions based on ideal MHD stability are generally in good agreement indicating that a high pressure gradient is a necessary but

not sufficient criterion to trigger an ELM of type I. At low pedestal resistivity, this pressure gradient can drive enough bootstrap current to destabilize intermediate-n external kink modes, which appear to be responsible for the type I ELMs.

B. Type III ELMs

The discharges from the set of H-modes with large type III ELMs are characterized by a pedestal resistivity low enough to use ideal MHD, in contrary to earlier high resistivity type III ELMy H-mode experiments mentioned above[22]. Fig. 11 shows the stability map of one of the discharges of the first case and includes the temporal evolution of the operational point during the ELM cycle. Since the pedestal displacement in the pre-ELM phase is marginal, it has not been included into the computation of the stability map.

Under conditions described by the stationary profile **A**, the operational point is not close to ideal MHD stability limits. Point **B** ($t - t_{ELM} = -1.50$ ms) shows an evolution of the operational point towards the limit of pressure-driven modes and, shortly before the ELM, the operational point **C** ($t - t_{ELM} = -0.23$ ms) is in the vicinity of the infinite-n ballooning mode limit. However, it remains unclear if the ELM is triggered by the ideal ballooning mode, since it is expected to be stabilized by diamagnetic effects. After the ELM event, point **D** ($t - t_{ELM} = 0.84$ ms), the normalized pressure α decreases to a finite value that is lower than at point **A**. As previously observed in Sec. IV, it is quite possible that a ST would sufficiently alter the pedestal properties such that high-n pressure-driven ballooning modes are destabilized.

Also for this type of discharges we find that the stability limits obtained from ideal MHD are in good agreement with the experimental observations. The pressure gradient in the pedestal is mainly limited by large-n pressure-driven modes with a narrow mode structure.

VII. CONCLUSION

In this paper, the temporal evolution of electron density and temperature profiles has been investigated during H-mode phases in the TCV tokamak with ELMs of type I and type III. Type I ELMs were obtained by additional heating using ECH at the 3^{rd} harmonic to reduce the collisionality near the edge. The cases with ELMs of type III refer to discharges with ohmic heating only and higher collisionalities. The profiles were measured by the TCV Thomson scattering system with high spatial resolution near the plasma edge. Since the inherent sampling rate of this diagnostic is not sufficient to follow the time evolution on a millisecond-scale during the ELM cycles, the method of random sampling and coherent averaging has been applied. For this purpose, time windows with constant plasma parameters have been selected from a series of reproducible shots. The results show similar trends to those observed on AUG[11] and DIII-D[35,45]. In particular, they indicate that the pedestal pressure gradient may saturate shortly before the ELM onset. From the observations it is concluded that a high pedestal pressure gradient is a necessary, but not a sufficient requirement for an ELM event.

The analysis has shown that the maximum pressure gradients predicted by ideal MHD stability calculations are in good agreement with experimental observations for different collisionalities of the plasma edge. At low collisionality and type I ELMs, it has been found that the pressure gradients are limited by low to medium-n kink-ballooning modes. At collisionalities that are higher by about a factor of two and type III ELMs, the limits are set by high-n ballooning modes.

The measurements also revealed a small but significant variation of the pedestal position with respect to the separatrix during the ELM cycle. Similar observations have been made during experiments on AUG. We find that for both types of ELMs, the collapse of the pedestal is followed by an outward motion of the gradient region. In the presence of strong ECH and type I ELMs, the pedestal moves inwards during the pre-ELM phase. These dynamic effects may lead to biased results, if time-averaged pressure profiles and equilibria are used as basis for the stability calculations. Since profile dynamics is not described by a simple scaling of the magnitude, the time evolution during the ELM cycle cannot be traced on a single stability diagram. However, if the analysis is based on individual profiles and equilibria for each time step, a closer agreement between the model and the observations is obtained.

ACKNOWLEDGMENTS

The authors would like to thank J. Paley running the TCV real time control system, Y. Andrebe for maintaining the Thomson scattering system, L. Federspiel providing CXRS measurements, M. Silva for supervising the X3-heating and T. Panis for discussing about the multiple facets of data processing.

This work was supported in part by the Swiss National Science Foundation.

REFERENCES

[1] Federici G, Loarte A and Strohmayer G 2003 *Plasma Phys. and Control. Fusion* **45** 1523
[2] Federici G 2006 *Phys. Scr.* **2006** 1
[3] Leonard A W 2008 *J. Phys.: Conf. Ser.* **123** 012001
[4] Oyama N 2008 *J. Phys.: Conf. Ser.* **123** 012002
[5] Maggi C F 2010 *Nucl. Fusion* **50** 066001
[6] Kirk A, Wilson H R, Akers R *et al.* 2005 *Plasma Phys. and Control. Fusion* **47** 315
[7] Kirk A, Counsell G F, Cunningham G *et al.* 2007 *Plasma Phys. and Control. Fusion* **49** 1259

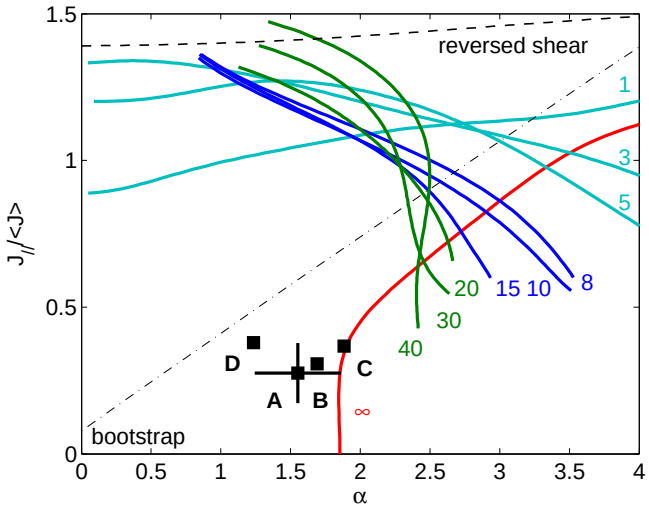

Figure 11. Ideal MHD stability map for H-mode plasma with type III ELMs: The phases during the ELM cycle are indicated by the points A-D with the relative times $t - t_{ELM}\{\mathrm{B,C,D}\} = \{-1.50, -0.23, +0.84\}$ ms in the ELM cycle.

[8] Beurskens M N A, Alfier A, Alper B *et al.* 2009 *Nucl. Fusion* **49** 125006

[9] Groebner R J, Osborne T H, Leonard A W *et al.* 2009 *Nucl. Fusion* **49** 045013

[10] Wolfrum E, Burckhart A, Fischer R *et al.* 2009 *Plasma Phys. and Control. Fusion* **51** 124057

[11] Burckhart A, Wolfrum E, Fischer R *et al.* 2010 *Plasma Phys. and Control. Fusion* **52** 105010

[12] Pitzschke A 2010 *Pedestal Characteristics and MHD Stability of H-Mode Plasmas in TCV* Ph.D. thesis École Polytechnique Fédérale Lausanne URL `http://library.epfl.ch/theses/?nr=4917`

[13] Connor J W, Hastie R J, Wilson H R *et al.* 1998 *Phys. of Plasmas* **5** 2687–2699

[14] Rogers B N and Drake J F 1999 *Phys. of Plasmas* **6** 2797–2803

[15] Huysmans G T A, Sharapov S E, Mikhailovskii A B *et al.* 2001 *Phys. of Plasmas* **8** 4292

[16] Snyder P B, Wilson H R, Ferron J R *et al.* 2002 *Phys. of Plasmas* **9** 2037–2043

[17] Medvedev S Y, Martynov A A, Martin Y R *et al.* 2006 *Plasma Phys. and Control. Fusion* **48** 927–938

[18] Groebner R J and Osborne T H 1998 *Phys. of Plasmas* **5** 1800–1806

[19] Hogge J P, Alberti S, Porte L *et al.* 2003 *Nucl. Fusion* **43** 1353

[20] Martin Y R and the TCV Team 2002 *Plasma Phys. and Control. Fusion* **44** A143

[21] Degtyarev L M, Martynov A A, Medvedev S Y *et al.* 1997 *Comp. Phys. Communic.* **103** 10–27

[22] Behn R, Alfier A, Medvedev S Y *et al.* 2007 *Plasma Phys. Control. Fusion* **49** 1289–1308

[23] Matsuda K 1989 *IEEE Trans. Plasma. Sci.* **17** 6–11

[24] Maslov M, Angioni C and Weisen H 2009 *Nucl. Fusion* **49** 075037

[25] Behn R, Franke S, Pietrzyk Z A *et al.* 1995 The Thomson Scattering Diagnostic on TCV *7th Int. Symp. on Laser-Aided Plasma Diagnostics, Fukuoka, Japan* pp 392–397

[26] Groebner R J, Baker D R, Burrell K H *et al.* 2001 *Nucl. Fusion* **41** 1789

[27] Kallenbach A, Dux R, Gafert J *et al.* 2003 *Nucl. Fusion* **43** 573

[28] Bortolon A 2009 *Plasma rotation and momentum transport studies in the TCV tokamak based on charge exchange spectroscopy measurements* Ph.D. thesis École Polytechnique Fédérale Lausanne URL `http://library.epfl.ch/theses/?nr=4569`

[29] Wagner D, Fable E, Pitzschke A *et al.* 2010 Particle transport in TCV H-modes *37th EPS Conf. on Plasma Physics, Dublin, Ireland* vol ECA 34A p P1.1101 URL `http://ocs.ciemat.es/EPS2010PAP/pdf/P1.1101.pdf`

[30] Alper B, Nave M, Huysmans G *et al.* 2004 Sawtooth Crashes at High Beta on JET *21st EPS Conf. on Control. Fusion and Plasma Physics, Montpellier, France* vol ECA 18B p 202 ff

[31] Kass T, Günter S, Maraschek M *et al.* 1998 *Nucl. Fusion* **38** 111

[32] Matsunaga G, Shinohara K, Aiba N *et al.* 2010 *Nucl. Fusion* **50** 084003

[33] de Meijere C A, Albergante M, Coda S *et al.* 2011 *to be published*

[34] Hofmann F and Jardin S C 1990 *Nucl. Fusion* **30** 2013

[35] Groebner R J, Leonard A W, Snyder P B *et al.* 2009 *Nucl. Fusion* **49** 085037

[36] Staebler G M, Hinton F L, Wiley J C *et al.* 1994 *Phys. of Plasmas* **1** 909

[37] Diamond P H, Lebedev V B, Newman D E *et al.* 1995 *Phys. of Plasmas* **2** 3685

[38] Pankin A Y, Voitsekhovitch I, Bateman G *et al.* 2005 *Plasma Phys. and Control. Fusion* **47** 483

[39] Luetjens H, Bondenson A and Sauter O 1996 *Comp. Phys. Communic.* **97** 216–260

[40] Medvedev S Y, Villard L, Degtyarev L M *et al.* 1993 MHD equilibrium and stability of doublet configurations *20th EPS Conf. on Control. Fusion and Plasma Physics, Lisbon, Portugal* vol ECA 17C p 1279ff

[41] Sauter O, Angioni C and Lin-Liu Y R 1999 *Phys. of Plasmas* **6** 2834–2839

[42] Hastie R J, Catto P J and Ramos J J 2000 *Phys. of Plasmas* **7** 4561

[43] Snyder P B, Groebner R J, Hughes J W *et al.* 2011 *Nucl. Fusion* **51** 103016

[44] Lönnroth J S, Parail V, Dnestrovskij A *et al.* 2004 *Plasma Phys. and Control. Fusion* **46** 1197

[45] Groebner R J, Snyder P B, Osborne T H *et al.* 2010 *Nucl. Fusion* **50** 064002